# Modeling parr-mark pattern formation during the early development of Amago trout

Chandrasekhar Venkataraman*
*Mathematics Institute, University of Warwick, Coventry CV4 7AL, United Kingdom*

Toshio Sekimura
*Department of Biological Chemistry, Graduate School of Bioscience and Biotechnology, Chubu University, Kasugai, Aichi 487-8501, Japan*

Eamonn A. Gaffney and Philip K. Maini
*Centre for Mathematical Biology, Mathematical Institute, University of Oxford, 24-29 St. Giles', Oxford OX1 3LB, United Kingdom*

Anotida Madzvamuse†
*Department of Mathematics, University of Sussex, Pev III, Brighton BN1 9QH, United Kingdom*
(Received 20 June 2011; revised manuscript received 29 July 2011; published 21 October 2011)

This paper studies the formation of the large dark patterns, known as parr marks, that form on the Amago trout as it grows from the early larval stages to adulthood. The Amago trout, known as *Oncorhynchus masou ishikawa*, exhibits stripes during the early stages of development that in turn evolve (through *reorientation and peak insertion*) to form zigzag spot patterns as the fish grows to adulthood. By considering a standard representation of the Turing model for biological self-organization via interacting and diffusing morphogens, we illustrate that a diffusively driven instability can generate transient patterns consistent with those experimentally observed during the process of parr-mark formation in the early development of the Amago trout. Surface evolution is modeled through an experimentally driven growth function. Our studies conclude that the surface evolution profile, the surface geometry, and the curvature are key factors that play a pivotal role in reaction-diffusion systems in a study motivated by observations of Amago trout parr-mark pattern formation.

DOI: 10.1103/PhysRevE.84.041923 PACS number(s): 87.18.Hf, 82.40.Ck

## I. INTRODUCTION

Modeling the formation of a spatial pattern from homogeneity is of fundamental importance in many fields, none more so than developmental biology. Since their seminal introduction by Turing [1], reaction-diffusion systems (RDSs) have constituted a standard framework for the mathematical modeling of spatial pattern formation. The theory behind RDSs as a model for biological pattern formation relies on two or more *morphogens* reacting in the presence of diffusion. The onset of a diffusion-driven instability causes the spatially homogeneous steady state of the morphogen concentration to become unstable leading to the possibility of spatial structure. Turing's hypothesis was that one or more of the morphogens played the role of a signaling chemical, such that cell fate is determined by levels of morphogen concentration.

Experimental studies have shown that patterns in real-world systems could indeed arise as a result of diffusion-driven instability, such as the chloride-iodide-malonic-acid reaction [2] and calcium-voltage dynamics within cardiac cells [3]. While aesthetically attractive due to its biological economy in solving the difficulties of orchestrating long-range cellular interactions to induce large-scale biological patterning, Turing's putative mechanism nonetheless is often considered with caution [4]. In particular, the required morphogen interactions are unverified at the molecular level, even if there are potential candidates such as Nodal and Lefty gene products during mesendodermal induction [5], and questions of model sensitivity continually recur [6–9]. In contrast, numerous observations of fish skin markings can be simply explained through reaction-diffusion frameworks emphasizing that fish pigmentation at least behaves analogously to an RDS. One example includes the work of Kondo and Asai [10], where it has been demonstrated that an RDS on a one-dimensional growing domain is consistent with stripe formation on the skin of the juvenile Pomacanthus. In a recent experimental study, Yamaguchi *et al.* [11] examined the effect of disrupting the stripe formation on zebrafish, and the pattern regime that ensued is very similar to the patterns obtained by computer simulation of an RDS with appropriate initial conditions. This in turn motivates further explorations of fish pigmentation to assess whether discrepancies between experimental and modeling results emerge, especially with modeling generalizations given the Turing instability's notorious sensitivity, as illustrated by the consideration of initial conditions on fixed domains. Previous observations of sensitivity to factors such as domain shape [12,13] suggest that the evolving, curved geometry characterizing fish skin as patterns dynamically change may increase the robustness of solutions to RDSs. Hence comparisons of models and observations in this context will offer a potential test of the theoretical framework.

The influence of curvature on pattern-formation processes governed by RDSs has been investigated in other contexts (for example by Barrio *et al.* [14]). However, the majority of studies of fish skin patterning by RDSs to date have simply considered model simulations on squares or other simple geometries. In this paper, we simulate an observed pattern-formation phenomenon in fish on *biologically realistic*

*Author to whom all correspondence should be addressed: c.venkataraman@warwick.ac.uk
†Author to whom all correspondence should be addressed: a.madzvamuse@sussex.ac.uk

 ©2011 American Physical Society

evolving surfaces, with the goal of investigating the influence of curvature on patterning. We shall use a finite-element method [15] to investigate the process of parr-mark pattern formation on the Amago trout [16].

The remainder of this paper is set out as follows: In Sec. II, we describe the process of parr-mark pattern formation on the Amago trout. We give the details of our experimental study, in which at each stage we observe the parr-mark formation process and record the time and size of the fish. In Sec. III, we outline the method with which we seek to model the pattern-formation process. Using our experimental data, we model the growth of the fish and construct representative models of the surface of the fish on which patterning occurs, taking into account the shape and curvature of the surface. We then define the RDS model that we will be computing on an evolving surface. We conclude the section by briefly discussing the selection of parameter values for the system. In Sec. IV, we present the results of our computer simulations. The results are in close agreement with the experimentally observed pattern transitions. The effect of curvature on the pattern-formation process is also discussed, and we observe striking differences in the patterns that form on surfaces with different curvature. Finally, in Sec. V we state the conclusions of this study, primarily that an RDS on an evolving surface is a viable model for describing the emergence of parr-mark pattern formation on the Amago trout and that curvature influences patterns that arise via self-organization. We conclude this paper by discussing the implications of our results on the modeling of biological pattern formation by RDSs on continuously evolving surfaces, and we suggest future research directions.

(a) Amago trout

(b) Whitespotted Char

(c) Rainbow trout

FIG. 1. (Color online) Parr marks on young fish skins of three different species of the Salmonidae.

## II. BIOLOGICAL OBSERVATIONS

The red spotted masu trout (*Oncorhynchus masou ishikawae*) of the Salmonidae has two different forms of life style, i.e., river resident and anadromous forms. The river resident form is known as the Amago trout and the anadromous form as the Satsukimasu trout. The life span of the red spotted masu trout is between 3 and 4 years. The final size of the Amago is fairly small (approximately 30 cm in length) and they are widely distributed in Japanese rivers from western Honshu island on the Pacific Ocean and Shikoku island, to northern Kyushu island on the Setonaikai Sea. The Amago is notable for remaining in fresh water during its life cycle. On the other hand, the size of Satsukimasu is approximately 50 cm long, and after living in the ocean for two years, they return to home rivers to lay eggs. Amagos have distinctive elliptically shaped parr marks (large dark patterns) on each side of the body, which are well known as trademarks of young fishes of the Salmonidae such as the Rainbow trout (*Oncorhynchus mykiss*) and the Whitespotted char (*Salvelinus leucomaenis*) (see Fig. 1) and may serve as camouflage for the vulnerable young fish. Amago trout parr mark development is completed relatively early in the fish's life cycle (6 to 7 months after hatching). Contrary to the parr marks of many other members of the Salmonidae, including the Satsukimasu trout, which disappear shortly after the juvenile phase, the parr marks once formed on the juvenile Amago remain fixed during development. Our modeling seeks to study the mechanism for the formation of parr marks on the skin surface of the Amago trout during the very early stages of its development from just after hatching to the completion of the formation of parr marks (at 6 or 7 months).

In order to understand the biological evolution of parr-mark formation during growth development, Sekimura recorded the parr-mark formation process of around 50 Amago individuals. The specimens were tracked from shortly after the time of hatching to around seven months after birth and were photographed at monthly intervals. The individuals were placed in a glass vessel with gradations on the sides of the vessel. This enabled the collection of experimental data of the growth rates of the fish, associated patterning, and geometrical descriptions during each stage of its growth development. These empirical data provide an excellent foundation for mathematical modeling of the pattern-formation phenomenon during growth development.

This study is, to our knowledge, the first attempt to document the parr-mark formation process that occurs on the developing Amago's surface. Parr-mark formation initiates via the formation of stripes oriented perpendicular to the head tail axis [16]. These stripes then split forming elongated spots on either side of the fish's back (dorsal portion), which develop and change in orientation as the fish grows. Our experimental study provides detailed observations of the major stages in parr-mark development during the early growth development, as shown in Fig. 2.

Stage 1: (Length: 2–4 cm, soon after hatching). No visible parr marks [Fig. 2(a)]. During this period, the Amago's diet consists only of yolk from its egg.

Stage 2: (Length: 4–6 cm, ∼1 month after hatching). The first stage of parr-mark formation occurs. Approximately five parr marks appear on each side of the fish toward the

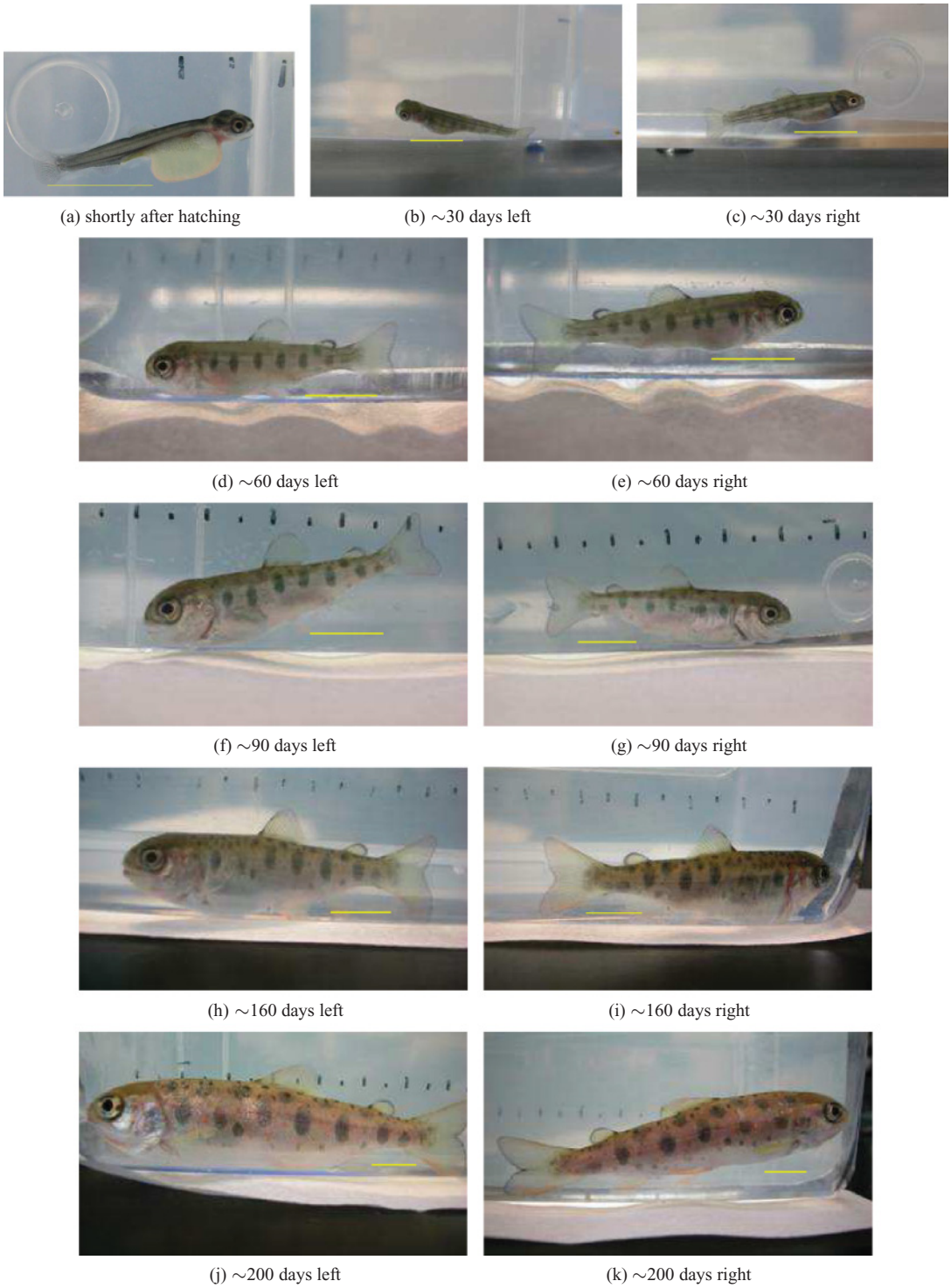

(a) shortly after hatching (b) ∼30 days left (c) ∼30 days right

(d) ∼60 days left (e) ∼60 days right

(f) ∼90 days left (g) ∼90 days right

(h) ∼160 days left (i) ∼160 days right

(j) ∼200 days left (k) ∼200 days right

FIG. 2. (Color online) Amago skin pigmentation patterning during growth development [the approximate time after hatching is given in the captions, and the yellow (light gray) bar in the bottom of each snapshot indicates 1 cm]. The figures show the left- and right-sided patterning profiles during the early stages of the Amago growth development after hatching to the juvenile period, by which time patterning is complete (approximately 6 to 7 months). The fish exhibits an initial patternless state that evolves into faint vertical stripes. It can be observed that stripes evolve into spots with zigzag alignment that increase in number as the fish grows. It must be noted that the fish size at 200 days has not reached the final maturity adult size. It is at this stage that the parr marks remain constant in number. The only changes observed are in the sizes of the spots, which continue to increase.

top (dorsal) portion. These are oriented perpendicular to the head-tail axis [Figs. 2(b) and 2(c)]. By this time, the fish has completely consumed its egg yolk and has started to eat food from the environment.

Stage 3: (Length: 6–8 cm, 2 to 3 months). By this stage of development, the fish has grown to around three to four times its original size. Between five and seven parr marks are visible on each side of the fish toward the top portion. The parr marks are still primarily oriented perpendicular to the head-tail axis, however on wider portions of the fish a zigzag pattern (see the next stage for a description) is somewhat evident [Figs. 2(d)–2(g)].

Stage 4: (Length: 8–12 cm, 3 to 7 months). A new line of parr marks appears on the top of the fish [Figs. 2(h)–2(k)]. The visible pattern consists of three or four rows (parallel to the head-tail axis) of elliptical parr marks, which are still all located on the top portion of the fish, with 7 to 11 parr marks in each row. The parr marks are now completely arranged in a zigzag configuration with the overall distribution of parr marks over the domain comprising a checkerboard pattern, i.e., the angle between a hypothetical line connecting a parr mark with its nearest neighbor and the head-tail axis is approximately 45°. Although the fish continues to grow, with the mature Amago measuring around 30 cm in length, the parr-mark formation process is completed by this time and the configuration visible on the juvenile fish persists into maturity.

During the later stages of the Amago growth development, the number of parr marks remains constant with noticeable changes in size and location over the fish surface. Our studies do not address the later stages of the Amago growth development since there are no major changes in parr-mark transitions.

It is clear from the observations that parr-mark pattern formation (or at least the expression of parr marks) is restricted to the upper (dorsal) portion of the fish, with no parr marks forming at any stage of development on the underside of the fish. A key facet of the parr-mark formation process is the insertion of new parr marks, inducing a transition from a single row of alternating pigmentation to multiple rows of elliptical markings that are in antiphase, forming a checkerboard pattern. The change in shape and organization of parr marks is extremely important, as any mechanism that governs the parr-mark formation process must allow for the change in organization of patterns as the fish changes in size. Figure 3 shows a top-down perspective of an individual Amago at around seven months after hatching. To highlight the parr marks, we have included a sketch with the parr marks and the outline of the fish shaded in dark black. We clearly observe the checkerboard pattern of parr marks that arises in the later stages of the juvenile parr-mark development.

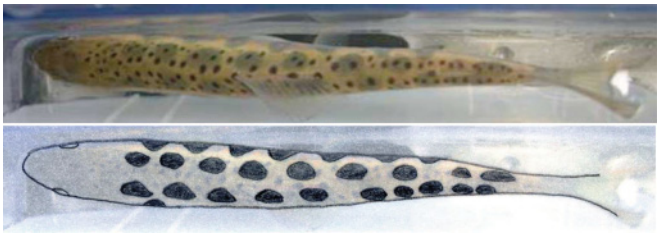

FIG. 3. (Color online) Top-down view of the patterned state of the juvenile Amago and a sketch of the patterned state on which we highlight the parr marks. A checkerboard pattern is clearly visible.

## III. MODELING

The experimental results shown above clearly demonstrate that the process of Amago skin pigmentation takes place during the early stages of development, with transient patterns being expressed as the fish grows to juvenile. The pattern transition occurs via the insertion of new parr marks. A certain separation seems to be maintained between the existing and inserted patterns. The orientation of the patterns around the domain is dynamic, changing as the surface evolves. These characteristics of the pattern-formation process suggest an RDS on an evolving surface as a candidate model for the pattern-formation phenomenon. First, since patterns that arise from RDSs via the Turing instability have an intrinsic wavelength, some degree of separation between patterns is natural (at least for kinetics in which new patterns arise via insertion). This has been used previously in modeling stripe formation on the Pomacanthus [10]. Secondly, and perhaps more importantly, more recent theoretical studies have shown that growth can determine the *orientation (direction)* of transient patterns [17]. This phenomenon of growth-determined packing arrangement of the markings has also been supported experimentally by Míguez and Muñuzuri [18], who showed that in a simplified experimental model for the formation of stripes on fish skin, the direction of domain growth could be used to determine the orientation of the resulting patterns.

We wish to investigate pattern formation on *realistic* geometries. Many studies, such as Varea *et al.* [19], Chaplain *et al.* [20], Plaza *et al.* [21], Gjorgjieva and Jacobsen [22], Barreira *et al.* [23], and Landsberg and Voigt [24], highlight the role of curvature on pattern formation. To properly understand the role geometry plays in the pattern-formation process, the curvature of the fish should also be taken into account, motivating the modeling of RDSs on *evolving curved surfaces*.

### A. Fitting a growth function to the experimental data

The experimental data allow us to estimate the surface proportions of the Amago trout through each observed stage of the parr-mark formation process. Using the photographs, we measure the length and width of the fish at various stages of development. The surface proportions of the Amago appear to grow isotropically, with no obvious change in the ratio between the width and length of the fish during development. In light of this, we assume the growth of the body surface of the fish is uniform and isotropic, i.e., the growth of the fish is assumed to be spatially linear and the fish grows at the same rate in all directions.

Another important aspect of the growth is that early in the fish's life cycle (when the fish is still feeding on its yolk), growth appears to be much faster than in later stages of development, when growth occurs at a much slower rate. The fish continues to grow after the juvenile stage, reaching a final size in adulthood of around 30 cm. However, the parr-mark formation process is complete once the fish has reached the juvenile stage corresponding to 10–13 cm in length, therefore further growth after this period is not modeled.

A saturating growth function seems the most natural model for the observed evolution of the fish's body surface. For illustrative purposes, we consider the *logistic growth function*. Under this growth profile, the fish's growth is approximately exponential initially, linear at intermediate stages, and finally saturates as the organism approaches a limiting surface size. The logistic growth function is defined by

$$\rho(t) = \frac{e^{rt}}{1 + \frac{1}{m}(e^{rt} - 1)} \quad \text{for} \quad t \in [0,T]\,. \tag{1}$$

Since we have assumed growth of the fish's surface is uniform and isotropic, the function $\rho(t)$ represents the time-dependent dilation that describes the uniform level of enlargement from the initial size of the fish to the current size of the fish. From our experimental observations, we take the saturation size $m = 5.2$ to represent the nondimensional limiting surface size of the Amago fish. Fitting the logistic growth function to the experimental data as illustrated in Fig. 4 results in the nondimensional linear logistic growth rate $r = 7.5 \times 10^{-5}$. We take a computational time interval of $[0,10^5]$, with one day in real time corresponding to an interval of length 500 in computational time. In Fig. 4 the growth function, $\rho(t)$, is fitted to the length of an individual Amago, with normalisation according to the initial length, over the interval [0,200 days]. The function (1) appears to be a relatively good approximation to the actual growth of the selected fish. We further note that the representative fish chosen in this case was fairly typical of the observed growth in many fish that were studied, and that the assumption of a logistic growth function is widely used in studies within this context [25]. Furthermore, as our assumption of isotropic growth is untested, our fitted growth function is merely indicative of a possible form of evolution of the fish surface, thus further fine-tuning and more refined fitting of the parameters of the growth function $\rho(t)$ to the observed growth of the fish surface appear to be unnecessary. As mentioned previously, the fish continues to grow after the juvenile stage. However, as the process of parr-mark formation is complete around 6 months after hatching, this subsequent growth is not modeled.

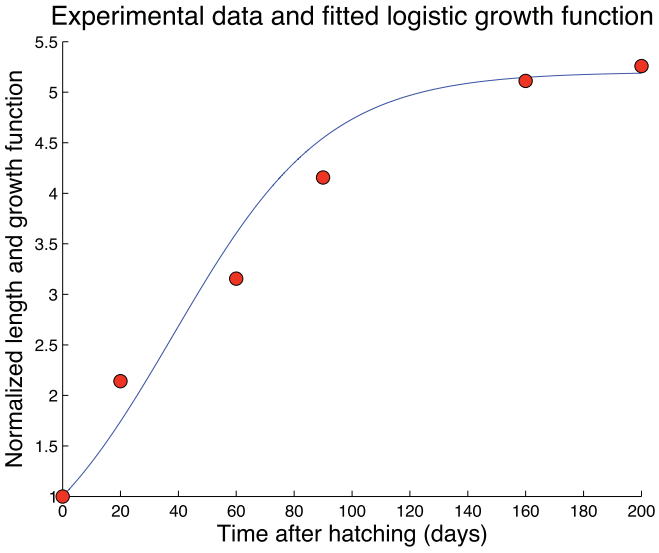


FIG. 4. (Color online) The red (dark gray) circles represent measurements of the length of an individual fish normalized by its initial length (∼2 cm) at 0, 20, 60, 90, 160, and 200 days after hatching. The blue (light gray) line represents logistic growth as defined in (1), on the computational time interval $[0,10^5]$ corresponding to a real time interval of [0,200] days. It must be noted that the parameters of the logistic function corresponding to experimental growth data for the rest of the fish follows more or less the same logistic growth profile (data not shown).

### B. Modeling the patterned surface

The absence of any pattern on the underside of the fish at all stages of development is apparent in Fig. 2. There appears to be a marked difference in coloration between the upper portion of the Amago on which patterns form and the patternless underside [most apparent in Figs. 2(h)–2(k)]. Recent experimental studies of the zebrafish have shown that some of the chromatophores (pigment cells) involved in the skin patterning of the fish originate from the neural crest on the dorsal (top) side of the fish and migrate to other parts of the fish in the embryonic state (see Kelsh [26] and references therein). This may explain the lack of patterning on the underside of the fish if the pathways along which the chromatophores migrate do not extend to the ventral side (bottom) of the fish. Marked differences in coloring between the top and bottom of the fish and the absence of patterning on the underside of the fish are evident in many members of the Salmonidae, such as the white spotted char and the masou salmon ([27], Figs. 2(a) and 2(b)). To the best of our knowledge, there is as yet no explanation for these phenomena in the Salmonidae, and this clearly warrants further experimental research.

Our assumption is that the morphogens and chromatophores are only present in the patterned regions of the fish and migrate only along pathways within this patterned region i.e., we assume the domain on which the chromatophores are present is limited and that these chromatophores are then triggered to produce a pattern by the RDSs that is posed on the same domain. From a modeling perspective, this is equivalent to assuming that there is no-flux of morphogens between the patterned and unpatterned regions. We therefore only consider the fish surface on which patterning occurs and impose a homogeneous Neumann boundary condition on the boundary surrounding this region.

To model the patterned region, we first trace the portion of the two-dimensional surface of the trout on which patterns form (Fig. 5). Using the gradations (1 cm) in each of the photographs, we measure the width and length of the outline of the fish. We assume the region is symmetric about the head-tail axis and we approximate the geometry at different stages of development by tracing the outline at different times after hatching. Our experimental observations indicate that the boundaries of the patterned portion of the fish enlarge proportionally as the fish grows. Since we assume the region as a whole grows proportionally with the fish, it is sufficient to model this surface at the initial stage of development with length and width scales that describe the skin surface of the Amago soon after hatching and then model the evolution of this surface during development with the isotropic growth function (1). To investigate whether curvature is relevant, we first model the surface by a *planar* polygonal domain,

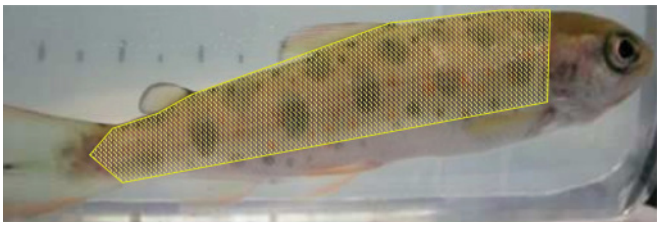

FIG. 5. (Color online) The portion of the fish that exhibits patterning, shaded in yellow (light gray). To construct an approximation to the surface of the Amago, we assume this region is symmetric about the head-tail axis of the fish and model the region by a series of surfaces with differing curvatures (Figs. 6 and 8).

approximating the shape of the patterned region. From inspection of the outline of the patterned region, a polygonal computational domain with 14 vertices provides a good approximation to the curved boundary of the patterned region. Figure 6 shows the initial planar computational domain, an approximation to the portion of the skin surface of the Amago on which patterns form (soon after hatching). We then investigate the influence of curvature by considering a series of computational domains with differing curvature while maintaining the width and length scales that are significant in the patterning process. In treating the domain on which patterning occurs as a two-dimensional manifold, we are introducing an approximation, as it is not necessarily true that the patterns occur in an infinitesimally thin layer. We assume that the patterning length scale is much larger than the depth of the fish skin. This is reasonable as, from fish cross-sections, skin depth is always far less than the patterning length scale (typically of the order of the size of the fish). Hence in the direction perpendicular to the modeled surface manifold, spatial homogeneity is expected and thus simulations on a two-dimensional manifold represent a legitimate approximation.

From inspection of the fish shape, a natural surface to investigate is a portion of a growing *elliptic cylinder*. The cylindrical surfaces we consider are defined by the following mapping that maps points from a time-independent planar reference configuration, which we take to be the coordinates of the initial planar computational domain shown in Fig. 6, to the growing surface of an elliptic cylinder (see Fig. 7):

$$\mathcal{A}(\boldsymbol{\xi},t) := \rho(t)\begin{pmatrix} a\cos(\pi\xi_1/0.45) \\ b\sin(\pi\xi_1/0.45) \\ \xi_2 \end{pmatrix}, \qquad (2)$$

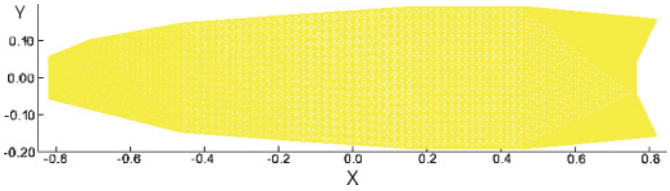


FIG. 6. (Color online) A planar approximation to the portion of the Amago trout on which patterns form. The length scales, in centimeters, represent the initial planar domain that corresponds to the surface of the Amago soon after hatching.

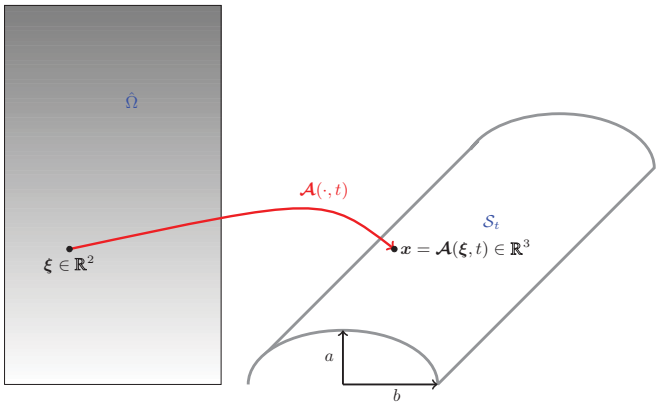


FIG. 7. (Color online) An example of the mapping $\mathcal{A}$ from a fixed planar computational domain to the surface of a growing elliptic cylinder.

where $\xi_1$ and $\xi_2$ are, respectively, the $y$ (width) and $x$ (length) coordinates of the planar approximation (see Fig. 6), $a$ and $b$ are the semimajor and semiminor axes of the elliptic cylinder, and $\rho(t)$ is the spatially uniform level of dilation from the initial surface size, given by the logistic growth function defined in Sec. III A.

Since the patterning only occurs on the upper portion of the fish, we model the surface by a portion of the curved surface of the elliptical cylinder (the top half of the cylinder, terminating at its widest location). We preserve the length and width scales of the fish by constructing cylinders with the same length and width (arc length across the curved surface) as the planar triangulation. To investigate the effect of differences in curvature on pattern formation, we pick a set of values of $a$ and $b$, such that the surface areas of the cylindrical surfaces obtained are approximately equal to the surface area of the planar domain.

Figure 8 shows the five different cylindrical surfaces we consider. The surfaces are shaded by the modulus of the cylindrical mean curvature, and ordered (left to right) by decreasing (modulus of) mean curvature along the central axis. The surface in the middle is the circular cylinder (of constant mean curvature).

### C. Model equations

We now introduce our model, an RDS on an evolving surface. Let $\mathcal{S}_t$ be a simply connected bounded continuously

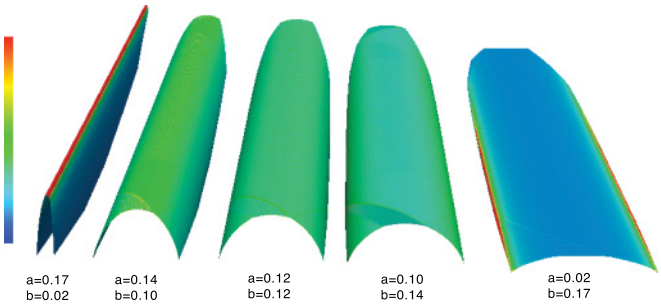


FIG. 8. (Color online) The cylindrical surfaces shaded by the modulus of the mean curvature.

deforming hypersurface embedded in $\mathbb{R}^3$ at time $t \in [0,T]$, $T > 0$. Let $\partial\mathcal{S}_t$ be the surface boundary of $\mathcal{S}_t$. Also let $\boldsymbol{u} = (u_1(\boldsymbol{x},t), u_2(\boldsymbol{x},t))^T$ be a vector of two chemical concentrations at position $\boldsymbol{x} \in \mathcal{S}_t$. Growth of the domain generates a flow velocity $\boldsymbol{a}(\boldsymbol{x},t)$, which we assume to be equal to the surface velocity. Assuming that surface velocity is isotropic, it can be easily shown that (see Madzvamuse [12] and Plaza *et al*. [21] for the details)

$$\boldsymbol{a}(\boldsymbol{x}(t),t) = \partial_t \rho(t)\boldsymbol{x}(0). \tag{3}$$

The generalized nondimensionalized governing equations for an RDS on an *isotropically growing surface* were derived by Plaza *et al*. [21] and take the form (see Appendix A1 or Barreira *et al*. [23] for further details)

$$\begin{aligned}
\partial_t u_1 + \nabla_{\mathcal{S}_t}\cdot(\boldsymbol{a}u_1) &= \Delta_{\mathcal{S}_t}u_1 + \gamma f_1(\boldsymbol{u}), \\
\partial_t u_2 + \nabla_{\mathcal{S}_t}\cdot(\boldsymbol{a}u_2) &= d\Delta_{\mathcal{S}_t}u_2 + \gamma f_2(\boldsymbol{u}) \quad \text{in } \mathcal{S}_t,(0,T], \\
\boldsymbol{u}(\boldsymbol{x},0) &= \boldsymbol{u}_0(\boldsymbol{x}), \qquad \boldsymbol{x} \in \mathcal{S}_0, \\
\nu\cdot\nabla_{\mathcal{S}_t}u(\boldsymbol{x},t) &= \boldsymbol{0}, \qquad \boldsymbol{x} \in \partial\mathcal{S}_t, t > 0,
\end{aligned} \tag{4}$$

where $d$ is the ratio of the diffusion coefficients, $\gamma$ is a scaling parameter, and $\boldsymbol{u}_0(\boldsymbol{x})$ is a well-defined positive bounded vector function. The vector $\boldsymbol{\nu}$ is the unit normal to the surface boundary $\partial\mathcal{S}_t$. The nonlinear vector valued function $\boldsymbol{f} = (f_1, f_2)^T$ represents the reaction kinetics. The only modification from the planar case is the replacement of spatial derivatives with surface tangential derivatives. We denote by $\Delta_{\mathcal{S}_t}$ the *Laplace-Beltrami* operator, the analog of the Laplace operator on manifolds, defined as the divergence of the surface tangential gradient [see Gilbarg and Trudinger [28] (Chap. 16, p. 389)]. If $\mathcal{S}_t$ is planar, then the Laplace-Beltrami operator is identical to the Laplacian. The global existence of classical solutions to RDSs on planar domains with isotropic growth was proved by Venkataraman *et al*. [29].

*Remark (i): Isotropic growth*. The assumption of isotropic growth plays a central role in the model derivation. Any form of anisotropy in the growth function will affect both the dilution term (that arises when the time derivative is brought inside the integral) and, crucially in this case, the curvature of the domain.

*Remark (ii): Alternative boundary conditions*. We note that without further empirical information, an equally appropriate modeling assumption would have been to assume that the RDS is posed on the entire surface of the fish and some external factor suppresses patterning on the underside of the fish. This alternative modeling assumption would have major implications, as we would then have to assume a domain with periodic boundaries at the sides and zero-flux boundaries at the head and tail ends or no boundary in the case of closed surfaces [23]. Boundary conditions strongly affect the pattern-formation process [30], and we shall show in the following sections that this effect is even more evident when curvature is included in the modeling. Further experimental evidence is needed to fully determine the appropriate boundary conditions to impose.

For our preliminary computational studies (not reported), we considered the *activator-depleted* substrate model [31–33] and the Thomas [34] reaction kinetics. One of the most important aspects of the patterning phenomenon is the insertion of new parr marks away from existing parr marks. This phenomenon is best captured by kinetics in which new activator peaks arise due to *insertion* rather than *splitting* of existing peaks. Bifurcations on growing domains with the *activator-depleted* substrate kinetics are generally of the splitting type, while the Thomas kinetics generally exhibit peak insertion [35]. This was evident in our preliminary simulations, and thus we focused on the Thomas kinetics defined in nondimensional form as follows:

$$\begin{aligned}
f_1(\boldsymbol{u}) &= \alpha - u_1 - \frac{\beta u_1 u_2}{\left(1 + u_1 + k u_2^2\right)}, \\
f_2(\boldsymbol{u}) &= c\kappa - c u_2 - \frac{\beta u_1 u_2}{\left(1 + u_1 + k u_1^2\right)},
\end{aligned} \tag{5}$$

where $\alpha$, $\beta$, $c$, $\kappa$, and $k$ are all positive constants. It must be noted that there are many other reaction kinetics in which peak splitting is observed, the celebrated Gierer-Meinhardt kinetics [31] being one of the most well known. Similar pattern transitions to those observed with the Thomas kinetics can arise as a result of different kinetic models in which peak insertion is the dominant process.

### D. Selection of parameter values

Since the morphogens that determine the patterning of the Amago trout are still unknown, the reaction kinetics we have assumed are purely hypothetical. In effect, we are assuming that patterning is insensitive to the physical details of the kinetics themselves, as similar patterns are generated by Turing systems with different reaction kinetics. Thus we determined the reaction kinetic parameter values by simulating an RDS on a fixed rectangle with the same length and width scale as the fish, selecting the parameter values that best approximate the first stage of patterning of the Amago. The parameter values we selected are $\alpha = 92$, $\kappa = 64$, $k = 0.1$, $c = 1.5$, $\beta = 18.5$, $d = 9.75$, and $\gamma = 116$. With these parameter values, system (4) admits a spatially homogeneous steady state (9.93,9.29) (determined by a Newton-Raphson method) valid in the absence of domain evolution. We take the initial conditions for problem (4) as small random perturbations around this homogeneous steady state.

On dimensionalization, using the fact that an interval of length 1 in computational time is equivalent to 173 s in real time, we obtain diffusion coefficients of approximately $5 \times 10^{-6}$ and $5 \times 10^{-5}$ cm$^2$ s$^{-1}$ for the activator ($u_1$) and inhibitor ($u_2$), respectively. However, within the range of diffusion coefficients of proteins in aqueous media, these diffusion coefficients are somewhat high compared to the typical value of diffusion coefficients of morphogens in the literature ($\approx 10^{-8}$ cm$^2$ s$^{-1}$). Rescaling such that the diffusion coefficients are of the experimentally observed orders results in a stiffer system that is more computationally intensive to solve. In light of this, we note that the nondimensional parameter $\gamma$ is not estimated from experimental data and governs the overall timescale of the reaction rates. Since growth of the domain occurs slowly relative to pattern formation, the transient patterns may be viewed as spatially inhomogeneous steady states of system (4) (neglecting the terms dependent on the slow growth rate). A suitable rescaling of the diffusion coefficients and the

parameter $\gamma$ should generate qualitatively similar patterning. This viewpoint is supported by our numerical investigations (not reported).

## IV. COMPUTER SIMULATIONS

We solve the model equations (4) and (5) using the finite-element method derived and analyzed by Venkataraman *et al.* [15]. We only present the computed activator concentrations ($u_1$); the inhibitor concentrations ($u_2$) have been omitted as they are in phase with those of the activator. Full details of the numerical methods are given in Appendix A2.

*Remark: Thresholding*. Since patterning is presumed to occur due to the morphogen concentration exceeding a certain value, the most appropriate way to visualize the results is by shading according to some threshold value. In all the simulations, we select a constant threshold value of 9.5 for

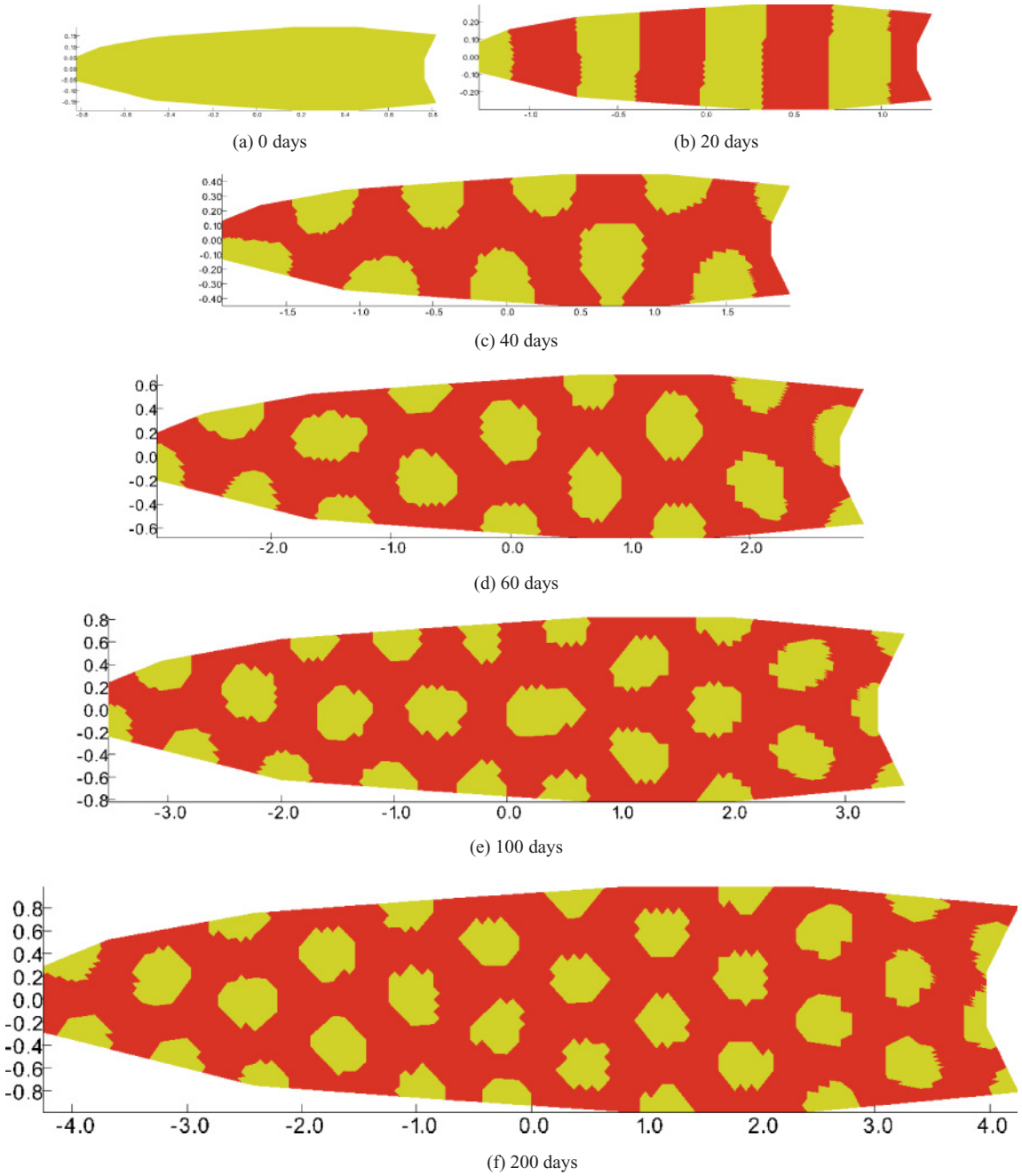

(a) 0 days (b) 20 days

(c) 40 days

(d) 60 days

(e) 100 days

(f) 200 days

FIG. 9. (Color online) Snapshots, shaded by a threshold algorithm, of the discrete activator concentration ($u_1$), corresponding to the simulation of (4) with reaction kinetics (5) on a planar domain. For parameter and thresholding values see text. The simulations are in agreement with the experimental observations reported in Fig. 2. The first pattern observed is a vertically aligned series of stripe-like parr marks with insertion of new parr marks as the domain grows. The parr marks reorient into a checkerboard configuration as the domain grows further. The number of parr marks visible at each stage of development is also in accordance with the experimental observations reported in Sec. II. These patterns are relatively independent of the threshold value selected.

the activator concentration ($u_1$). If the concentration is below this value, the area of the domain is shaded red (dark gray), otherwise it is yellow (light gray). The Thomas kinetics we have used exhibit sharp gradients compared to say the Schnakenberg kinetics with similar diffusion coefficients; also, the results of our simulations suggest that the patterns that form with these parameter values are spots or stripes with a common amplitude (results not shown). Thus the gross pattern exhibited is relatively independent of the threshold value chosen. Although the results of the simulations appear to be relatively pixelated, this is only an artefact of the thresholding algorithm. The mesh was refined sufficiently to ensure that further refinements led to only minor changes in the solution values and qualitatively the patterns expressed did not change.

### A. Planar domain

Figure 9 shows the results of our simulation of (4) with reaction kinetics (5) on the planar domain. We have shown snapshots of the computed activator concentrations ($u_1$), together with the corresponding time in days of each snapshot. The pattern transitions observed in the computer simulations are in close agreement with the transient patterns observed in Fig. 2.

The snapshots of the simulation results at 20 and 40 days after hatching [Figs. 9(b) and 9(c)] are very similar to the first parr marks that appear on the surface of the Amago toward the end of the first month [Figs. 2(b) and 2(c)]. At this stage of development, four to five parr marks are visible along each side aligned vertically, in agreement with the experimental observations. As the computational domain grows corresponding to 60 days after hatching, new parr marks appear via insertion; see Fig. 9(d). The alignment is still primarily vertical, although in the wider portions of the domain a zigzag orientation starts to appear, mirroring the experimental results in Figs. 2(d) and 2(e). Further insertion of parr marks and the transition to the checkerboard configuration observed experimentally in Figs. 2(f)–2(i) are clearly observable in Fig. 9(e) as the computational domain grows. In Fig. 9(f), we show the final patterned state as the domain reaches the size at which patterns no longer change. We observe three to four rows (parallel to the head-tail axis) of parr marks, each consisting of around 10 individual parr marks. The regular checkerboard distribution of the parr marks is clearly evident, and comparing this figure with the top-down view of Fig. 3, we see a close agreement between the final distribution of parr marks in the simulation and the observations.

The times of transition between different patterns also appear to be in accordance with the observed data, with the transition from stripe-like parr marks aligned perpendicular to the head-tail axis to the checkerboard distribution of parr marks occurring between the second and fourth month after hatching both in the biological observations and the numerical simulations.

### B. Cylindrical surfaces

Figure 10 shows the transient patterns of the activator profile, together with the corresponding time in days of each snapshot on the cylindrical surfaces. Each snapshot is arranged from bottom to top in order of increasing (modulus of) mean curvature along the central axis.

The pattern transition on the portion of the circular cylinder (middle surface) is an important benchmark for the algorithm. By construction, the portion of the circular cylinder we have considered is *isometric* to the planar domain. The Laplace-Beltrami operator is invariant under isometries as it is defined by the surface metric tensor or first fundamental form (see the Appendix for further details), which is invariant under isometries [36]. Therefore, the eigenfunctions of the Laplace-Beltrami operator on the surface of the circular cylinder under consideration are homeomorphic to the eigenfunctions of the Laplace operator on the planar domain. Moreover, given identical initial conditions, the patterns observed on the circular cylinder should be the same as the patterns observed in the planar case. Comparing Fig. 9 and the circular cylinder (middle surface) in Fig. 10, we see extremely similar patterning despite the use of different initial conditions and the fact that we use different numerical schemes (A9) and (A10) that are only equivalent up to quadrature.

Generally speaking, the activator profiles on the middle three surfaces of Fig. 10 are similar to the planar case with parr marks initially appearing in a vertical alignment and then reorienting into the checkerboard configuration as the surface grows. The time at which patterns first form appears to be the same both in the planar case and on all the surfaces we have considered. This is in accordance with the work of Plaza *et al*. [21], in which it was shown that the necessary conditions for diffusion-driven instability are the same on surfaces as on planar domains. We do, however, observe differences in the type of pattern expressed on the different surfaces due to the differing surface geometries. On the surface with least mean curvature along the central axis (bottom), there is a clear preference for vertical stripes (perpendicular to the head-tail axis), with the only observed pattern transition being the regular insertion of stripes as the surface grows. This is surprising as in the planar case isotropic growth would eventually lead to the reorientation of stripes or the breakdown of the stripe pattern altogether. On the surface with highest curvature along the central axis (top), there is a clear preference for spots.

Overall, the number of spots (or stripes) at a given time on the surfaces in Fig. 10 appears to increase with increasing mean curvature along the central axis, i.e., as we move from the lower-most surface in each figure panel to upper-most surface. It therefore appears that on surfaces with higher curvature on the interior and smaller curvature at the boundary, patterns with higher mode numbers (number of spots or stripes) are selected.

## V. CONCLUSION AND DISCUSSION

Understanding the formation of a spatial pattern in the early embryo is one of the central challenges in developmental biology. By virtue of their accessibility, pigmentation patterns offer a powerful paradigm model in which to propose and test various patterning hypotheses. Recent experimental evidence suggests that skin patterning in some species of fish is dynamic [11], i.e., fish skin patterning can be transient long after the larval stage. Fish are therefore ideally suited to the study of pattern formation as experimentalists are now able to collect data on the dynamic pattern-formation behavior from the early stages of development to adulthood. In this study, we explored

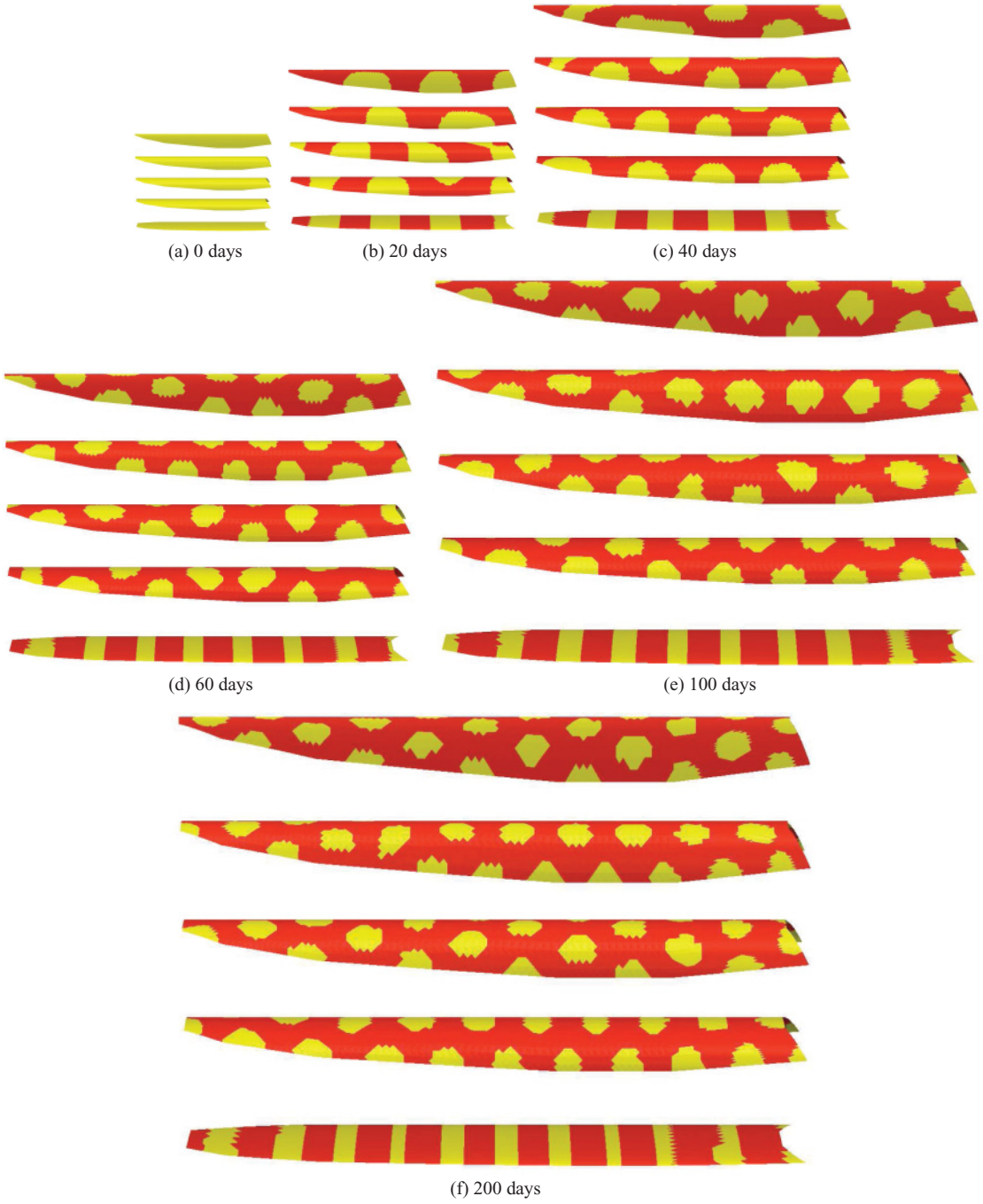


FIG. 10. (Color online) Snapshots, shaded by a threshold algorithm, of the discrete activator concentration ($u_1$), corresponding to the simulation of (4) with reaction kinetics (5) on cylindrical surfaces. For parameter and thresholding values, see the text. The timing of the formation of the first patterns is identical to the planar case (Fig. 9). The patterning on the middle three surfaces appears to be very similar to the planar case and approximates well the observed experimental results. A striking result is the preference of stripe-like patterns with vertical alignment on the surfaces with higher curvature on the boundaries (bottom) with spots in zigzag alignment appearing to be preferred on surfaces with higher curvature along the central axis (top). (Note that the surfaces reading from left to right in Fig. 8 correspond to the surfaces reading from top to bottom in each of the subfigures.)

a reaction-diffusion model for the experimentally observed parr-mark pattern-formation process in the early development of the Amago trout. The geometrical assumptions we made were driven for the most part by the experimental data, and an important facet of our study is the inclusion of curved surface geometry and the modeling of surface evolution of the fish. Our results show that there is an agreement between the observed evolution of parr marks on the surface of the Amago trout and the simulated patterning generated by an RDS on a planar domain. This is equivalent to assuming the surface of the Amago is accurately modeled by an isotropically growing circular cylinder as evident in simulations conducted on the middle surface in Fig. 10. Furthermore, weakly elliptical cylinders that constitute small departures from the uniform

curvature of the circular cylinder generate similar patterning (Fig. 10, second from top and second from bottom surfaces). This striking result suggests small changes in curvature may not significantly influence the pattern-formation process, and this was not apparent *a priori*. Thus studying the effects of curvature was an important aspect of the research. The pattern-formation mechanism investigated consists of an RDS posed on a continuously evolving open curvilinear surface. The simulations indicate the importance of curvature in determining the patterns generated by RDSs, and our overall conclusion is that the Turing mechanism is not inconsistent with the observed parr-mark pigmentation dynamics.

The use of computer simulations of RDSs in conjunction with experimental data to approximate observed skin patterning in fish is widespread [10,27,37]. The key difference between our study and existing work is that, to the best of our knowledge, this is one of the first studies that incorporates *experimentally driven modeling of growth and curvilinear geometry.* We have shown that patterns generated by an RDS can replicate experimentally observed pattern transitions, where both the growth and domain geometry are *observed experimentally and modeled mathematically*.

Our results indicate that curvature influences patterns that arise via self-organization. For the Thomas reaction kinetics, the gross behavior of solutions to the RDS posed on evolving surfaces is similar to the planar case with the insertion of new activator peaks as the surface evolves. However, in terms of the type of pattern generated, there does appear to be a significant sensitivity to the curvilinear geometry of the domain. In contrast to the sensitivity of RDSs to initial conditions, the sensitivity to curvature does not appear to be ameliorated by domain evolution. We observe markedly different transient patterns on cylindrical surfaces with similar surface areas and evolution but differing nonuniform curvatures. These differences are entirely due to the geometry of surfaces with nonuniform curvature, in particular the eigenfunctions of the Laplace-Beltrami operator posed on these surfaces, at least for pattern initiation while in the linear regime. Future numerical and theoretical studies with the goal of identifying or characterizing these eigenfunctions appear to be of fundamental importance. On a circular cylinder, we observe similar transient patterns to the planar case, with an initial striped pattern evolving into a spotted pattern, whereas on an evolving cylindrical surface with higher curvature on the boundary, we observe the persistence of stripes oriented perpendicular to the boundaries (where curvature is high) and no two-dimensional patterning (spots); the pattern transitions take the form of regular stripe insertion throughout the evolution. In light of this, further numerical investigation of the generality of these types of behaviors in RDSs posed on surfaces (other than cylinders) is warranted. Another striking result we observe is that on surfaces with higher curvature in the interior and smaller curvature at the boundary, higher pattern modes are initially selected. This raises questions about the effect of curvature on wave numbers of patterns that arise due to diffusion-driven instability, and the linear stability analysis of RDSs posed on surfaces is an important area for future work.

Our results also suggest that differences in curvature may explain some of the differences in patterning on different regions of the body surface of organisms. A tentative initial prediction we can make from the numerical results is that (at least with the reaction kinetics and cylindrical surfaces we have considered) should be preferred on regions of an organism that are more "fin-like". Consider, for example, a fish that has a striped back (dorsal portion) and spotted sides. Ogawa [38] accounts for this type of patterning by proposing a new model of diffusion on surfaces, where surface diffusion is obtained as an $\epsilon$ (surface thickness) expansion, which, unlike the standard surface-diffusion case, leads to a diffusive surface flow with an explicit curvature dependence. Our results suggest that this difference in patterning may be explained if the back was more "fin-like" than the sides and also that the back and sides were effectively separate surfaces with a boundary condition at their intersection. This may explain the striped dorsal regions and spotted sides evident in many fish, such as the Char fish. We observe the persistence of a striped pattern with a fixed stripe orientation on a growing surface [the surface with least mean curvature along the central axis (bottom) in Fig. 10]. Curvature may therefore provide an explanation for the persistence of striped patterns with a fixed orientation on growing organisms should RDSs account for skin patterning. This is an alternative hypothesis to existing studies that propose that stripe orientation in fish patterning during growth is fixed by anisotropic diffusion due to physical properties of the scales [39,40].

We have concentrated only on modeling the early development of the parr-mark pattern-formation process. After parr-mark development is completed, new patterns, specifically small black and red circular spots, appear in rows parallel to the head-tail axis [Figs. 2(j) and 2(k)]. These new patterns generally arise around the existing parr marks. One possible extension to the model to account for this new patterning is along the lines of the model considered by Barrio *et al*. [37]. They assumed a model consisting of two RDSs coupled such that the patterned state of the first system acted as a source of morphogens for the second system. The results of their simulations are similar to the new patterns observed on the Amago with new spots forming around existing spots. An important area for future work is the investigation of "semiscale invariance" (or lack thereof) in patterning. By semiscale invariance, we mean that large-scale features of Turing patterns, such as the number of spots and stripes, and also their size, are insensitive to relatively small variations in domain size, at least away from bifurcations, as illustrated in the study of Crampin *et al*. [41]. This will be the subject of future empirical and theoretical studies, as this is a core Turing-like feature exhibited in fish markings. Despite the fact that parr marks are visible on many different species of Salmonidae, the process of parr-mark formation is still not widely studied. We hope that our work will motivate future experimental studies into this interesting phenomenon, involving the effects of perturbing patterns on the developing fish and genetic investigations into the process.

There has been a plethora of recent experimental studies designed to examine the postulate of an RDS as the underlying mechanism behind patterning in fish. For example, McClure and McCune [42] suggest that variation in patterning between zebrafish species may arise as a result of varying growth rates. Our work fits into this framework in that we have shown

that experimental observations of the growth and patterning of a specific species of fish are broadly approximated by an RDS on an evolving surface. The theoretical study of RDSs provides important insight as to the likely behavior of patterns formed by them and thus acts as an important experimental guide in hypothesis differentiation, given numerous competing hypotheses for pigmentation patterning in fish skin. It seems highly unlikely that either mathematical or experimental advances in isolation will lead to conclusive proof of the mechanism behind pattern formation. An integrative approach appears to be the way forward.

## ACKNOWLEDGMENTS

The research of C.V. has been supported by the British Engineering and Physical Sciences Research Council (EPSRC), Grant No. EP/G010404. A.M. and P.K.M. would like to acknowledge support from the EPSRC grant *Mathematical modeling of spatial patterning on evolving surfaces (EP/H020349/1)* and an LMS grant (R4P2), both of which were in support of the visit by Professor T. Sekimura. P.K.M. was partially supported by a Royal Society Wolfson Research Merit Award. A.M. was partially supported by the British Council through its UK-US New Partnership Fund as part of the Strategic Alliances and Partnerships strand of the Prime Minister's Initiative for International Education 2 (PMI2).

## APPENDIX: SOLVING REACTION-DIFFUSION SYSTEMS ON EVOLVING SURFACES

### 1. A Lagrangian FEM for parametrizable surfaces

The model equations for a generalised reaction-diffusion system on an evolving surface $\mathcal{S}_t$ can be written as [21,23]

$$\frac{d}{dt}\int_{\mathcal{S}_t} u_i d\mathcal{S}_t = \int_{\mathcal{S}_t} d_i \nabla_{\mathcal{S}_t}\cdot(\nabla_{\mathcal{S}_t} u_i) + f_i(\boldsymbol{u}) d\mathcal{S}_t. \quad \text{(A1)}$$

We assume the surface $\mathcal{S}_t$ is parametrizable and denote by

$$\mathcal{A} : \mathbb{R}^2 \times [0,T] \to \mathbb{R}^3 \quad \text{(A2)}$$

the parametrization. Formally, we assume there exists a reference domain $\hat{\Omega} \subset \mathbb{R}^2$ such that at each instant $t \in [0,T]$ and for each $\boldsymbol{x} \in \mathcal{S}_t$ there exists a $\boldsymbol{\xi} \in \hat{\Omega}$ such that

$$\boldsymbol{\mathcal{A}}(\boldsymbol{\xi},t) = \boldsymbol{x}. \quad \text{(A3)}$$

Moreover, we assume the parametrization defined by $\boldsymbol{\mathcal{A}}$ is orthogonal, i.e.,

$$\partial_{\xi_1}\boldsymbol{\mathcal{A}} \cdot \partial_{\xi_2}\boldsymbol{\mathcal{A}} = 0 \text{ in } \hat{\Omega} \times [0,T]. \quad \text{(A4)}$$

To construct a finite-element method to approximate the solution on parametrizable surfaces, we need the following elementary facts from differential geometry (see, for example, Do Carmo [36]). The *area element* of $\mathcal{S}_t$ is given by

$$\mathrm{d}\mathcal{S}_t = \left|\partial_{\xi_1}\boldsymbol{\mathcal{A}}\right| \left|\partial_{\xi_2}\boldsymbol{\mathcal{A}}\right|. \quad \text{(A5)}$$

Letting $\hat{u}_i(\boldsymbol{\xi},t) = u_i(\boldsymbol{\mathcal{A}}(\boldsymbol{\xi},t),t)$ then, since the parametrization is orthogonal (A4), the Laplace-Beltrami operator can be expressed on the reference frame as (see Xu [43] [(2.3)])

$$\nabla_{\mathcal{S}_t}\cdot(\nabla_{\mathcal{S}_t} u_i) = \nabla_{\boldsymbol{\xi}}\cdot(\boldsymbol{G}^{-1}\nabla_{\boldsymbol{\xi}}\hat{u}_i), \quad \text{(A6)}$$

where the matrix $\boldsymbol{G}$ is the matrix of coefficients of the *first fundamental form*:

$$\boldsymbol{G} = \begin{bmatrix} \left|\partial_{\xi_1}\boldsymbol{\mathcal{A}}\right|^2 & 0 \\ 0 & \left|\partial_{\xi_2}\boldsymbol{\mathcal{A}}\right|^2 \end{bmatrix}. \quad \text{(A7)}$$

Changing variables in (A1), we obtain the following expression on the reference frame:

$$\frac{\mathrm{d}}{\mathrm{d}t}\int_{\hat{\Omega}} \hat{u}_i |\partial_{\xi_1}\boldsymbol{\mathcal{A}}||\partial_{\xi_2}\boldsymbol{\mathcal{A}}| = \int_{\hat{\Omega}} [d_i \nabla_{\boldsymbol{\xi}}\cdot(\boldsymbol{G}^{-1}\nabla_{\boldsymbol{\xi}} u_i) + f_i(\boldsymbol{u})]|\partial_{\xi_1}\boldsymbol{\mathcal{A}}||\partial_{\xi_2}\boldsymbol{\mathcal{A}}|. \quad \text{(A8)}$$

We use the Lagrangian finite-element method derived by Venkataraman *et al.* [15] to approximate $\hat{\boldsymbol{u}}$.

### 2. Numerical methods

Considering the nondimensional RDS (4), we employ a Galerkin finite-element method for the spatial approximation and an implicit-explicit modified backward Euler scheme for the time integration of the RDSs. For the simulations on planar domains, we use a moving finite-element method [15], which aims to find $U_1^n, U_2^n \in \mathbb{V}^n, n = 1,\ldots,N$ such that

$$\begin{aligned} \frac{1}{\tau}\langle U_1^n,\Psi^n\rangle + 1\langle \nabla U_1^n,\nabla\Psi^n\rangle &= \gamma\left\langle \alpha - U_1^n - \frac{\beta U_2^{n-1}U_1^n}{1+\left(1+kU_1^{n-1}\right)U_1^{n-1}},\Psi^n\right\rangle + \frac{1}{\tau}\langle U_1^{n-1},\Psi^{n-1}\rangle, \\ \frac{1}{\tau}\langle U_2^n,\Psi^n\rangle + d\langle \nabla U_2^n,\nabla\Psi^n\rangle &= \gamma\left\langle c\kappa - cV_1^n - \frac{\beta U_1^{n-1}U_2^n}{1+\left(1+kU_1^{n-1}\right)U_1^{n-1}},\Psi^n\right\rangle + \frac{1}{\tau}\langle U_2^{n-1},\Psi^{n-1}\rangle \end{aligned} \quad \text{(A9)}$$

for all $\Psi^n \in \mathbb{V}^n, n = 1,\ldots,N$, where $\tau$ is the uniform time step.

For the simulations on surfaces, the finite-element method we used aims to find $\hat{U}_1^n, \hat{U}_2^n \in \hat{\mathbb{V}}$, such that

$$\begin{aligned} \frac{1}{\tau}\langle [J\hat{U}_1]^n - [J\hat{U}_1]^{n-1},\hat{\Psi}\rangle + 1\langle [J\boldsymbol{K}]^n\nabla\hat{U}_1^n,\boldsymbol{K}^n\nabla\hat{\Psi}\rangle &= \gamma\left\langle \alpha - \hat{U}_1^n - \frac{\beta\hat{U}_2^{n-1}\hat{U}_1^n}{1+\left(1+k\hat{U}_1^{n-1}\right)\hat{U}_1^{n-1}},J^n\hat{\Psi}\right\rangle, \\ \frac{1}{\tau}\langle [J\hat{U}_2]^n - [J\hat{U}_2]^{n-1},\hat{\Psi}\rangle + d\langle [J\boldsymbol{K}]^n\nabla\hat{U}_2^n,\boldsymbol{K}^n\nabla\hat{\Psi}\rangle &= \gamma\left\langle c\kappa - c\hat{U}_2^n - \frac{\beta\hat{U}_1^{n-1}\hat{U}_2^n}{1+\left(1+k\hat{U}_1^{n-1}\right)\hat{U}_1^{n-1}},J^n\hat{\Psi}\right\rangle \end{aligned} \quad \text{(A10)}$$

for all $\hat{\Psi} \in \hat{\mathbb{V}}$, where $\tau$ is the uniform time step.

The matrix $\boldsymbol{K}$ and the determinant of the Jacobian $J$ are given by

$$\boldsymbol{K} = \begin{bmatrix} \frac{1}{|\partial_{\xi_1}\boldsymbol{\mathcal{A}}|} & 0 \\ 0 & \frac{1}{|\partial_{\xi_2}\boldsymbol{\mathcal{A}}|} \end{bmatrix}, \tag{A11}$$

$$\text{and} \quad J = \left|\partial_{\xi_1}\boldsymbol{\mathcal{A}}\right| \left|\partial_{\xi_2}\boldsymbol{\mathcal{A}}\right|. \tag{A12}$$

In both cases, the finite-element spaces were made up of piecewise linear basis functions. The initial data were approximated using the Lagrange interpolant. The linear systems were solved using the conjugate gradient algorithm. In both cases, we took an initial triangulation $\mathcal{T}^0$ with 6897 nodes and a fixed time step of $10^{-2}$.


[1] A. M. Turing, Philos. Trans. R. Soc. London, Ser. B **237**, 37 (1952).
[2] R. Vigil, Q. Ouyang, and H. Swinney, Physica A **188**, 17 (1992).
[3] Y. Shiferaw and A. Karma, Proc. Natl. Acad. Sci. USA **103**, 5670 (2006).
[4] M. Kerszberg and L. Wolpert, Cell **130**, 205 (2007).
[5] L. Solnica-Krezel, Curr. Biol. **13**, R7 (2003).
[6] J. Bard and I. Lauder, J. Theor. Biol. **45**, 501 (1974).
[7] B. Bunow, J. Kernevez, G. Joly, and D. Thomas, J. Theor. Biol. **84**, 629 (1980).
[8] S. Seirin Lee, E. A. Gaffney, and N. A. M. Monk, Bull. Math. Biol. **72**, 2139 (2010).
[9] S. Seirin Lee and E. A. Gaffney, Bull. Math. Biol. **72**, 2161 (2010).
[10] S. Kondo and R. Asai, Nature (London) **376**, 765 (1995).
[11] M. Yamaguchi, E. Yoshimoto, and S. Kondo, Proc. Natl. Acad. Sci. USA **104**, 4790 (2007).
[12] A. Madzvamuse, D.Phil. thesis, University of Oxford, 2000.
[13] T. Sekimura, A. Madzvamuse, A. Wathen, and P. K. Maini, Proc. R. Soc. B: Biol. Sci. **267**, 851 (2000).
[14] R. Barrio, A. Hernández-Machado, C. Varea, J. Romero-Arias, and E. Álvarez-Buylla, PloS one **5**, 112 (2010).
[15] C. Venkataraman, Ph.D. thesis, University of Sussex, 2011.
[16] T. Sekimura, in *Abstracts, SMB-JSMB Joint Meeting* (San Jose, CA, 2007), pp. 48 and 49.
[17] A. Madzvamuse, A. Wathen, and P. K. Maini, J. Comput. Phys. **190**, 478 (2003).
[18] D. Míguez and A. Muñuzuri, Biophys. Chem. **124**, 161 (2006).
[19] C. Varea, J. L. Aragon, and R. A. Barrio, Phys. Rev. E **60**, 4588 (1999).
[20] M. Chaplain, M. Ganesh, and I. Graham, J. Math. Biol. **42**, 387 (2001).
[21] R. Plaza, F. Sánchez-Garduño, P. Padilla, R. Barrio, and P. K. Maini, J. Dyn. Dif. Eq. **16**, 1093 (2004).
[22] J. Gjorgjieva and J. Jacobsen, Dyn. Syst. **2007**, 436 (2007), Special Issue.
[23] R. Barreira, C. Elliott, and A. Madzvamuse, J. Math. Biol. 1, Online first (2011).
[24] C. Landsberg and A. Voigt, Comput. Visual. Sci. **13**, 177 (2010).
[25] N. Gershenfeld, *The Nature of Mathematical Modeling*, Vol. 1 (Cambridge University Press, Cambridge, New York, 1999).
[26] R. Kelsh, Pigment Cell Res. **17**, 326 (2004).
[27] S. Miyazawa, M. Okamoto, and S. Kondo, Nature Commun. **1**, 1 (2010).
[28] D. Gilbarg and N. Trudinger, *Elliptic Partial Differential Equations of Second Order* (Springer Verlag, Berlin, 2001).
[29] C. Venkataraman, O. Lakkis, and A. Madzvamuse, J. Math. Biol. 1, Online first (2011).
[30] P. Arcuri and J. Murray, J. Math. Biol. **24**, 141 (1986).
[31] A. Gierer and H. Meinhardt, Biol. Cybern. **12**, 30 (1972).
[32] R. Lefever and I. Prigogine, J. Chem. Phys. **48**, 1695 (1968).
[33] J. Schnakenberg, J. Theor. Biol. **81**, 389 (1979).
[34] D. Thomas, in *Analysis and Control of Immobilized Enzyme Systems*, edited by Thomas and Kernevez (North Holland, 1976), pp. 115–150.
[35] E. Crampin, D.Phil. thesis, University of Oxford, 2000.
[36] M. P. Do Carmo, *Differential Geometry of Curves and Surfaces*, Vol. 2 (Prentice-Hall Englewood Cliffs, NJ, 1976).
[37] R. A. Barrio, R. E. Baker, B. Vaughan Jr., K. Tribuzy, M. R. de Carvalho, R. Bassanezi, and P. K. Maini, Phys. Rev. E **79**, 31908 (2009).
[38] N. Ogawa, Phys. Rev. E **81**, 61113 (2010).
[39] H. Shoji, Y. Iwasa, A. Mochizuki, and S. Kondo, J. Theor. Biol. **214**, 549 (2002).
[40] H. Shoji and Y. Iwasa, FORMA-TOKYO **18**, 3 (2003).
[41] E. Crampin, E. Gaffney, and P. K. Maini, Bull. Math. Biol. **61**, 1093 (1999).
[42] M. McClure and A. McCune, Evolution **57**, 1863 (2003).
[43] G. Xu, Comp. Aided Geometric Design **21**, 767 (2004).